Directly Probing Surfactant Adsorption on Nanoscopic Trenches and Pillars

JJ Hamon, Rico F. Tabor [a], Alberto Striolo [b], and Brian P. Grady*

School of Chemical, Biological and Materials Engineering and Institute of Applied Surfactant Research, University of Oklahoma, Norman, Oklahoma 73019. [a]School of Chemistry, Monash University, Clayton, Victoria,3800, Australia. [b] Department of Chemical Engineering, University College London, London WC1E 7JE, United Kingdom. * Corresponding author; Phone 405-325-4369, fax 405-325-5813

Email Addresses: JJ Hamon: jjhamon16@gmail.com, Rico Tabor: rico.f.tabor@gmail.com, Alberto Striolo: a.striolo@ucl.ac.uk, Brian Grady, bpgrady@ou.edu
*Corresponding Author

Abstract

Hypothesis

Confinement causes a change in the amount of surfactant adsorbed and adsorption morphology.

Experiments

Two cationic surfactants, tetradecyltrimethylammonium bromide (TTAB) and cetylpyridinium chloride (CPC) were adsorbed at the silica-water interface. Atomic force microscopy (AFM) force curves were measured on 50 nm and 80 nm wide trenches. Force curves were also measured on silica pillars, and the results were quantified based on distance from the edge.

Findings

Trenches: Adsorbed surfactants films in 50 nm and 80 nm trenches showed the same break-through values. However, compared to unconfined values, TTAB in trenches had decreased break-through and adhesion forces while CPC in trenches had increased break-through and adhesion forces, indicating that surfactant identity varies the confinement effect.

Pillars: Near the edge, few surfactants adsorb, and those that do stretch in the direction normal to the surface. While the experimental data agree qualitatively with previous coarse-grained molecular dynamic simulations, the length scales at which the phenomena are detected differ by ~ half-order of magnitude. Specifically, experimental data show measurable effects on adsorbed surfactant morphology at a distance from the edge 10-20 times the length of a surfactant molecule after accounting for the ~8 nm size of the probe.

Keywords: Surfactant, adsorption, atomic force microscopy, force curves, silica, tetradecyltrimethylammonium bromide, cetylpyridinium chloride, cationic surfactant

Introduction

How surface roughness affects surfactant adsorption is of interest in areas such as oil recovery, surface cleaning, corrosion-resistant coatings and many others. Surface roughness can be thought of as of topological variations with approximately random variations in the sizes and shapes of the areas available for surfactants to adsorb. Studies using ellipsometry, neutron reflectivity, quartz-crystal microbalance (QCM), and atomic force microscopy (AFM) have demonstrated that increasing roughness on a nanoscopic scale decreases the amount of surfactant adsorbed per area (and sometimes the total amount adsorbed) and can also alter surfactant morphology on various surfaces like gold and silica.[2-8] Specifically, a change in roughness from 0.6 nm to 1.4 nm led to a ~10% decrease in total amount adsorbed in one neutron reflectivity study,[2] and in another a change in roughness from 2.3 nm to 5.8 nm caused about the same ~10% decrease in total amount adsorbed in a QCM study.[4]

Effects of regular (or controlled) topological variations have been investigated primarily using simulations, where surfactants can be confined on surfaces with dimensions on the order of a few surfactant molecule lengths. Work performed by Tummala et al. showed that the aggregate morphology of surfactant adsorbed on carbon nanotubes was dependent on the diameter of the nanotube, which agreed with neutron reflectivity experiments.[9] Tummala also investigated surfactant adsorption on graphene nano-sheets and nano-ribbons, which showed that as the diameter of a ~10 nm graphene decreased the effects of the lateral confinement became more pronounced, specifically at the edges of the confined area where the headgroups of the adsorbed surfactant oriented themselves radially towards solution.[10]

Coarse-grained simulations by Suttipong et al. were performed using trenches of varying depths of a few nanometers, which demonstrated that the morphology of the aggregates adsorbed

within the trench varied with trench depth and in some cases multiple morphologies could form within the same trench.[11] Also, when the floor of the trench was changed to a surfactant repellant material, the morphology of the aggregates closest to the floor shifted to accommodate the new, less optimal interactions. Suttipong et al. then performed simulations involving surfactant adsorption to stripes with varying horizontal widths of a few nanometers and steps with a hydrophobic surface width of 0.46 surfactant lengths and with varying vertical heights.[12] On stripes, decreasing the width led to an increase in both the curvature of the aggregates and the density of head groups at the stripe edge. On steps, the edge was noted to cause the surfactant layer to be stretched and thinned (less dense compared to that formed on a flat homogeneous substrate). If the step height was large enough, then the surfactant layer would not adsorb to the step to avoid an energy penalty associated with bending the layer across the edge; the same result would have occurred if the width were increased to a large enough value relative to the height. These findings agree with the conclusion drawn by Tummala, in that the effects of confinement appeared to be most apparent at the edges of confining structures. However, any effects beyond a few surfactant lengths (~7 nm) were not observed.

Effects of topological variations were observed experimentally at much larger distances in the work of Marquez et al., who used nanosphere lithography on highly-ordered pyrolytic graphite and template assisted admicellar polymerization to create nanostructures with different sized polystyrene nanospheres, which caused confinement both laterally and vertically.[13] Continuous honeycomb structures formed when using spheres larger than 500 nm while smaller spheres yielded discontinuous spikes; in all cases the polymer film was not completely filling the interstitial void space. A simple geometric argument revealed that the polymer-sphere separation

distance varied between 4 nm and 250 nm, depending on nanoparticle size. By contrast, adsorbing polymer filled the interstitial spaces up to the thickness of the polymer film.

This work experimentally investigates the effects of regular topological variations on surfactant adsorption, e.g. the distance between variations is well-characterized. The confining walls of nanoscopic trenches and the edges of nanoscopic pillars are perhaps the most extreme examples of topological variations. Of the techniques used to study surfactant adsorption, AFM gives the most localized information regarding adsorbed surfactant morphologies through techniques such as 'soft contact' imaging and force curve mapping (force mapping).

Soft contact imaging is performed by gliding the tip over the adsorbed layer at a constant repulsive force generated by the electrical double layer of ionic surfactants, or repulsive steric interactions of nonionic surfactants.[14-22] The movement and normal force of the tip must be carefully controlled in order to obtain an image, and it should be noted that slight changes in the underlying surface height (i.e., surface roughness) can be enough to cause the tip to push through the adsorbed layer. However, in spite of the difficulty, Schniepp et al. were able to obtain striking AFM images of surfactant adsorbed to rough gold surfaces with grains 3-7 nm high and showed that changes in surface topography changed the aggregates from well-packed parallel rows to poorly-packed, disorganized worm-like micelles.[8, 23]

While soft contact imaging provides qualitative surfactant morphological information, force curves provide z-direction information in the form of the break-through distance, break-through force and adhesion force. In a recent publication, we showed that spatial information regarding the adsorbed surfactant layer stability and location can be obtained by mapping these values.[1] In the current work, AFM force mapping was used to characterize surfactant adsorbed on molecularly smooth surfaces at the bottom of nanoscopic trenches and at the top of

nanoscopic pillars. Break-through values were compared to break-through event values of surfactants adsorbed on flat surfaces with large dimensions to isolate the effects of topological variations on the adsorbed surfactant.

Materials and Methods

Surfactant Preparation

Critical micelle concentrations (CMCs) of the two surfactants were measured using the pendant drop method and no minima in the interfacial tension vs concentration curve were observed, indicating a relatively pure surfactant. Cationic tetradecyltrimethylammonium bromide (TTAB: $CH_3(CH_2)_{13}N(CH_3)_3^+Br^-$), obtained from Sigma-Aldrich as ≥98% purity, was recrystallized three times from ethanol before use. Cationic cetylpyridinium chloride (CPC: $CH_3(CH_2)_{15}N(C_5H_5)^+Cl^-$),), from Sigma-Aldrich at as 98-102% purity, was used as received. Ionic surfactants were chosen because cooperativity effects are usually greater vs. nonionics and these cationics were chosen because they can be obtained commercially in relatively pure form. More discussion of surfactant choice and the effects of impurities are found in the Supplementary Information (SI). CMCs of TTAB and CPC were found to be 3.52±0.43 mM, and 0.96±0.16 mM, respectively. All AFM force curve data was collected using 10×CMC of each respective surfactant.

Atomic Force Microscopy

Soft Contact Imaging

AFM images of adsorbed, unconfined surfactant were collected using the soft contact method either with a JPK Nanowizard III or using an Asylum Cypher equipped with the blueDrive oscillation accessory. For the former, a PPP-BSI AFM probe (force constant ~0.1 N/m, NanoAndMore) with a radius of curvature less than <10 nm as specified by the

manufacturer was used. While using the blueDrive images were obtained using a BL-AC40TS tip (Asylum) with a spring constant of 0.2 N/m. Prior to use in each imaging session, the probe was cleaned in a UV ozone chamber for 10 minutes.

Soft contact imaging was attempted on the top of the pillars but because of technical difficulties, we were unable to collect soft contact images in these areas. Likely, the change in height from the floor to the pillar upper surface was too large and abrupt to keep the probe stable above the surfactant layer. Soft contact imaging was not performed on trench bottoms because only one direction could be mapped.

Force Mapping and AFM Imaging of Trenches and Pillars

The force mapping feature of the Nanowizard was used to obtain a 32×32 grid of force curves in desired areas with varying map sizes. Force mapping, and other imaging, was performed using a specialty high aspect ratio version of the PPP-BSI probe which had a 300 nm long spike in place of its normal tip (see Figure 1 in SI). This spike allowed for imaging within the high-aspect ratio trenches, as well as to better identify the edges of the pillars without the effects of a pyramidal AFM tip. Before use, each probe was calibrated to determine deflection sensitivity and force constant by obtaining a force curve on a clean microscope slide and fitting the gradient (slope) of the line where the probe was in contact and then by using the thermal method, respectively. No UV-Ozone cleaning was performed prior to use because this treatment significantly reduced the probe's aspect ratio; instead, probes were soaked in ethanol for 5 minutes and then DI water for 5 minutes before use. Probes were used only if the measured force constant fell within the specification parameters (roughly 5 % of the probes did not meet this criterion). Deflection sensitivity was measured again in solution on the substrate prior to any surfactant topology measurements to account for the different refractive index of the liquid.

Figure 1 shows a force curve obtained in an aqueous medium containing surfactant. This graph appears in a recent publication by our group and is reproduced here for clarity.[1] The approach curve in Figure 1 shows a repulsive force beginning at approximately 15 nm (generated by the electrical double layer near the surfactant assembly) and ending with an instability at ~4 nm. Following the instability, the probe is in contact with the substrate underneath the surfactant layer. The force at which the instability occurs is designated the break-through force while the distance between the instability point and the substrate is designated the break-through distance. Each force curve within a force map was obtained with a tip velocity of 700 nm/s and over a range of 500 nm. The relative force setpoint (the force at which extension of the probe was stopped and retraction begun) was varied based on the force required to obtain enough points post break-through to determine if constant contact had been achieved, usually between 3 nN and 8 nN.

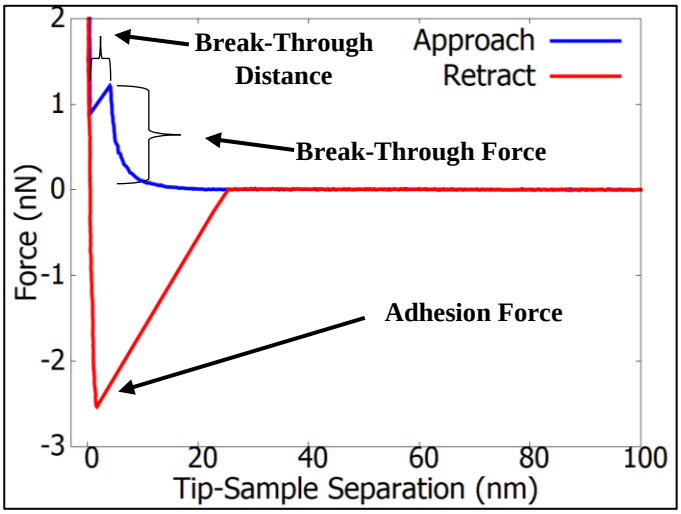

Figure 1. Diagram identifying key parts of AFM force curves in surfactant solution. A similar figure appears in Reference [1].

Once the probe reached this setpoint, it was retracted from the surface. Due to adhesive forces between the surface and the probe, there was a distance during which the probe remained on the surface past the point of zero deflection. A snap-off the surface occurred once the force necessary to overcome adhesion was applied and resulted in a minimum in the force curve, which was taken as the adhesion force. In a force curve, a negative force is attractive, however,

both the break-through force and adhesion force will be given as positive values given the typical conventions.

Automated Analysis Post Collection (Python and Gaussian Fitting)

"JPKSPM Data Processing" software was used to convert the gathered deflection and distance data into force and tip–sample separation before exporting each curve as a separate text file. Force curves were then analyzed using scripts developed in Python, which first separated the data into approach (extend) and retract curves and then identified the break-through points to obtain break-through distance, break-through force, and adhesion force. In the case of the trenches, collected values were analyzed using a histogram analysis which assumes that all positions are equivalent. For silica pillar samples each set of break-through event values were then coupled with their respective map point (grid location) to obtain break-through distance, break-through force and adhesion maps.

Surface Preparation

Silica Cleaning

Silica used for trench and pillar fabrication were cleaned using the procedure summarized in what follows. Ellipsometry standards with a known silica layer thickness of 58 nm (thermally grown oxide layer) were obtained from J.A. Woolam Inc. A single ellipsometry standard was cleaved into 1 cm x 1 cm pieces which were then cleaned using a methanol soak with sonication to remove any particles present on the surface from the cleaving procedure. DI water was used to rinse the samples, which were dried in a nitrogen stream. Next, the silica pieces were placed in a Harrick Plasma Cleaner (PDC-32G) and cleaned using the medium setting (10.5 W applied to RF coil) in air for 10 minutes. Pieces were then transferred to an 80°C RCA-1 cleaning solution (1:1:5 solution of NH_4OH:H_2O_2: Milli-Q H_2O) for 25 minutes in a Teflon© sample holder and then rinsed individually with Milli-Q H_2O and dried under a nitrogen stream and immediately

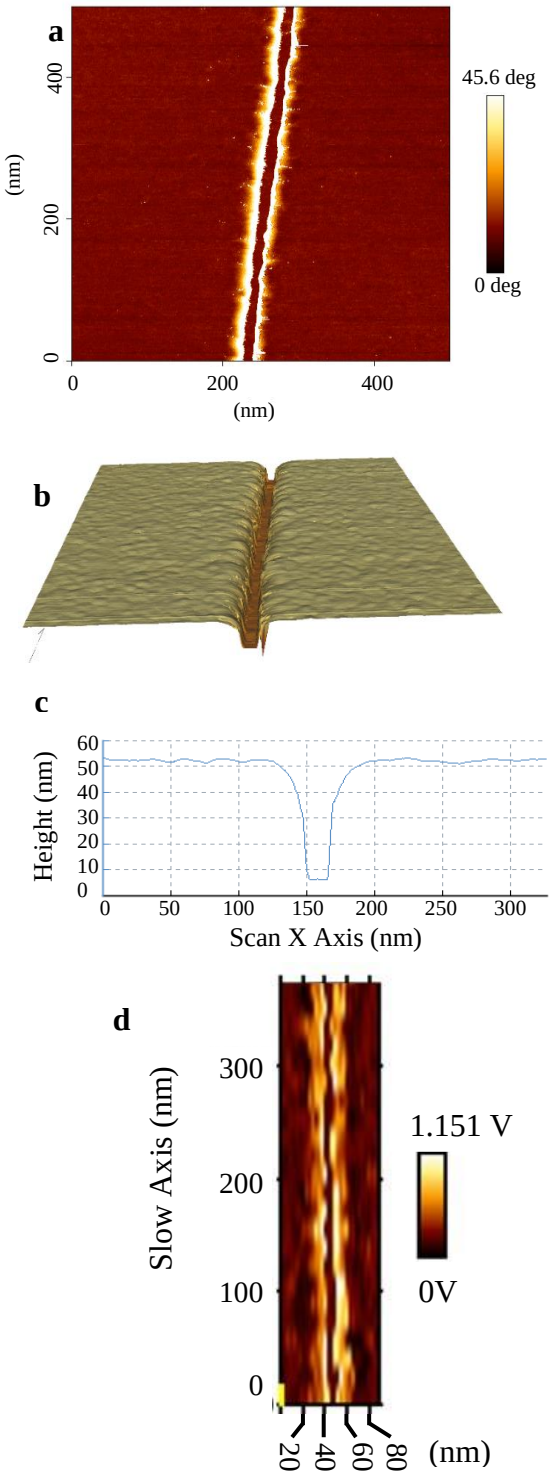

Figure 2. (a) AFM phase signal image collected in air of a 50 nm trench created in PMMA using e-beam lithography (EBL). (b) A 3D model of the created using the phase image. (c) A line profile from the height signal of the same scan. (d) Adhesion map of 50 nm trench in air.

moved to the plasma cleaner for 5 minutes on the low setting (6.8 W applied to RF coil). Finally, silica pieces were placed in fluoroware storage containers for a minimum of 24 hours to allow the hydrophobicity of the surfaces (which was decreasing over time) to equilibrate before use.

Trench Fabrication and Characterization

Confining a surfactant in a trench structure was a challenge due to the nanoscale dimensions needed for comparison to simulations. For this task, e-beam lithography (EBL) was used to create laterally confining trenches as well as larger areas in ~50 nm thick spin-coated poly(methyl methacrylate) (PMMA) polymer. The hundreds of nanometers open areas were produced in the same manner as the trenches and were large enough that confinement effects could be ignored. These large areas therefore served as control areas for comparison against data collected in the trenches.

The cured PMMA surface after EBL was characterized via the sessile drop method; the contact angle of DI water on the spin-coated

polymer surface was found to be 71.9°±1.2°. More thorough details of trench manufacture are provided in Supplementary Information.

Although trenches of various widths were investigated, ultimately trenches of 2 sizes were chosen for these experiments, 50 nm wide and 80 nm wide. These were chosen because 50 nm trenches were the smallest widths where the trench floor could be reached by the AFM probe; 80 nm was the largest width before the beam dose began to cause cross linking of the PMMA and removal from the surface became unreliable.

The results of using AFM intermittent contact mode imaging and force mapping AFM to image one of the a 50 nm width trenches are shown in Figure 2, which displays an AFM phase signal image, 3D model, a height profile, and a force map, respectively. Attempts were made to characterize the PMMA removal from the trench floor using force curve information, but it was found that bare PMMA and silica (in air or pure water without surfactant adsorption) display similar snap-to-contact and adhesion values so this measurement could not be used to distinguish the identity of the bottom of the trench. The widths of the upper mouth of the trench (~50 nm from the line profile in Figure 2c) were statistically the same as the widths determined by metal lift-off experiments at the bottom of each trench (see SI) suggesting nearly complete removal of the PMMA from the trench floor and a mostly vertical trench wall/square wall-floor intersection.

Due to the finite size of the tip, the exact nature of the polymer wall-silica floor intersection could not be precisely determined. However, force maps were able to distinguish the upper surface of the polymer, the edges, and the lower surface of the trench from each other (see Figure 2d). The lower surface of the trench spans 2-3 points in the width dimension at the center of the trench. Overall, the map provides 50-60 points to analyze over the length of the trench. Hence, we considered all points imaged in a trench to be equivalent.

Pillar Fabrication and Characterization

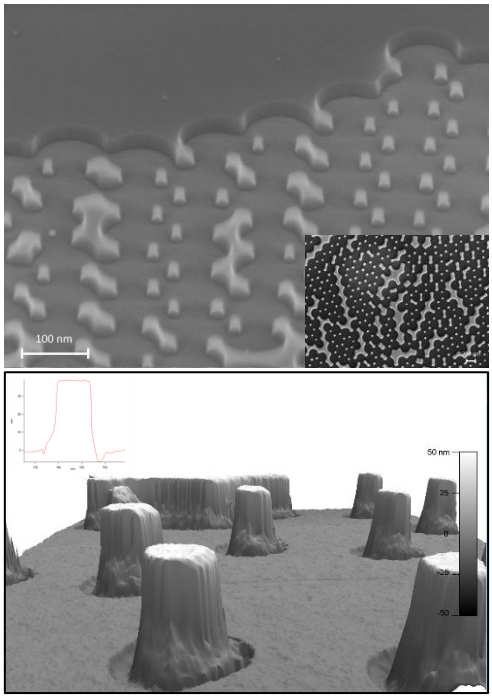

Figure 3. Results of 30 second reactive ion etching (RIE) performed with 200 nm diameter polystyrene nanospheres. Upper image is SEM and lower image is AFM. Inset in lower image is given in Supporting Information in a larger image for the interested reader.

Pillars were fabricated by reactive ion etching (RIE) of a silica surface coated with 200 nm polystyrene spheres that had been enlarged with heat. Chrome was then selectively evaporated into the interstitial sites of the enlarged spheres before removing the spheres via a toluene soak with sonication. RIE created pillars in the areas where the metal was on the surface during the etching. Then, the original silica surface on the tops of the pillars was obtained by etching the metal with CR 9051 chrome etchant (obtained from Transene Co.). For further details regarding the preparation of the pillar surfaces, we refer to the Supporting Information.

The upper image in Figure 3 shows a distribution of nano-structures, including dumbbell shapes, stretched zig-zag patterns and peninsula-like formations extending from larger islands. The wide variety of shapes were caused by defects in the nanosphere mask. SEM images often appeared blurry around the edges of the structures because the SEM electron interaction volume was larger than the width of the features, leading to ‘edge effects’ and a decrease in edge contrast. However, vertical side walls are apparent, indicating a mostly anisotropic etch.

Further characterization of the pillars was performed using AFM with high aspect ratio tips (described in the following section), the results of which are given in the lower image in Figure 3. This 3D model of the surface demonstrates the high-resolution capabilities of these specialty tips. Although the structures appear to have striated walls, because all the structures

show this same feature on only the right side, we conclude the striation is an imaging artifact. AFM imaging supports the conclusions drawn from SEM regarding the vertical nature of the substrate sidewalls, and it also supports the existence of a flat upper pillar surface. The roughness of the 'upper' surfaces (previously masked by metal) was found to be 0.18 ± 0.02 nm while that of an unprocessed silica surface was found to be 0.17 ± 0.01 nm, indicating the surface was well protected during RIE.

Results and Discussion

Soft contact imaging

Soft contact imaging was used to collect images of 2×CMC TTAB on unprocessed silica using the JPK Nanowizard III. The image in Figure 4a (reproduced from our recent publication [1] and repeated here for continuity) is a deflection signal and was scanned from bottom to top; the force setpoint was increased until disorganized bundles of wormlike micelles became visible at around the 150 nm mark. There was some difficulty in acquiring images of these surfactant aggregates on silica, as the probe did not remain stably above them long enough, despite several attempts. The reason for this difficulty is thought to be that the force required to image the surfactant aggregates was too close to the break-through force to allow for sustained soft contact imaging. Attempts to acquire the same image on the Asylum Cypher were unsuccessful.

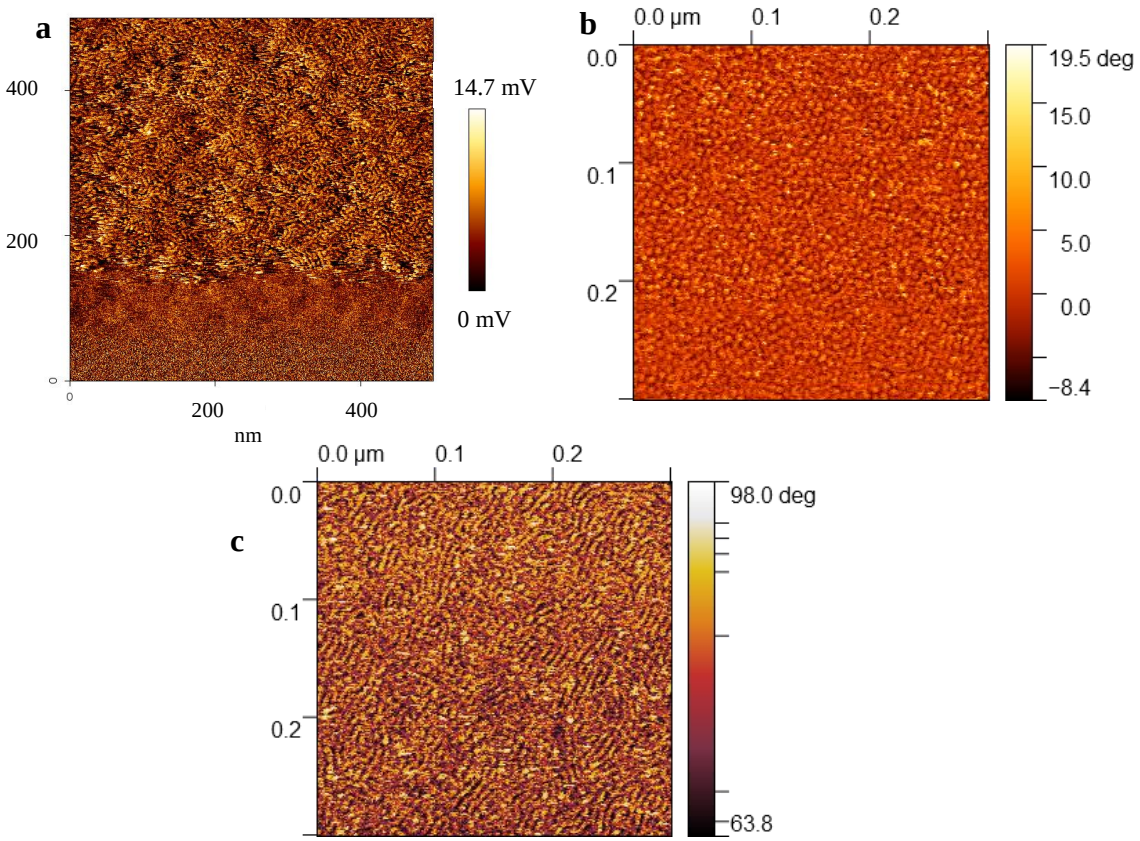

Figure 4. AFM images collected using the soft contact imaging method with (a) 2×CMC TTAB (referenced from [1]), (b) 10×CMC CPC at 20 minutes surfactant immersion and (c) 35 minutes surfactant immersion on silica. The TTAB image was collected using the JPK Nanowizard III while the CPC images were collected using an Asylum Cypher.

An Asylum Cypher with blueDrive technology was used to collect phase images of 10×CMC CPC aggregates on silica, shown in Figure 4b and Figure 4c. After 20 minutes immersion in CPC, the aggregates were spherical, noted by the circular dots in Figure 7b. However, after 15 additional minutes in solution, the aggregate morphology changed to worm-like micelles, seen as the disorganized rod like structures in Figure 4c. The morphology remained unchanged after another hour of imaging, suggesting the worm-like micelles were the equilibrium structure. We are unsure of the reason for this shift in morphology, but one possible explanation could be that the hydrophilicity of the silica acquired from the UV Ozone cleaning was changing, causing the aggregate morphology to shift as well. Force maps were collected after at least 35 minutes in solution to eliminate any temporal effects on the surface aggregates.

Several attempts were made to characterize a surfactant layer on the PMMA surface with soft contact imaging, but were ultimately unsuccessful. The difficulty in imaging on PMMA is perhaps due to the nature of the surfactant layer on that surface, which had a small break-through force making the tip-surfactant layer force interaction unstable and allowing the tip to easily break through the layer to the PMMA underneath. This issue is discussed further below.

Force curve comparison with previous work

Force maps on unconfined silica were collected and analyzed at 10×CMC TTAB using the procedure described in a previous publication by our group.[1] UV-Ozone cleaned silica had break-through distance values between 3.5 nm and 4.0 nm, while the break-through force values varied from 1.1 nN to 0.1 nN; the adhesion force values varied from 2.2 nN to 0.18 nN. Previously, we showed that break-through distance varied with concentration below the CMC but did not vary with concentration above the CMC and was independent of surface and or tip characteristics. Break-through and adhesion forces did vary with tip characteristics and can only be compared when the tip is identical, i.e. no tip cleaning between trials. Therefore, values on single surfaces (polymer, trench, and control area values) can be compared, but unconfined clean silica values cannot be quantitatively compared, except with respect to break-through distance. In other words, all graphs contain trench data from single surfaces so that values can be directly compared, i.e. there are more distance comparisons than force comparisons.

Trenches

10×CMC TTAB-PMMA

One concern was that the polymer would not remain stable immersed in the surfactant solution. However, PMMA showed no noticeable degradation during data collection. Longer times in solution were tested and at ~5 hours small bubbles would develop at the surface of the polymer. Hence, data shown here was collected in less than 3 hours of sample immersion.

Example force curves from unconfined PMMA and at the bottom of the 50 nm trench are shown in Figure 5a and Figure 5b, respectively. Break-through events occurred in both locations, indicating adsorbed surfactant with a stable structure able to resist the force of the AFM probe.

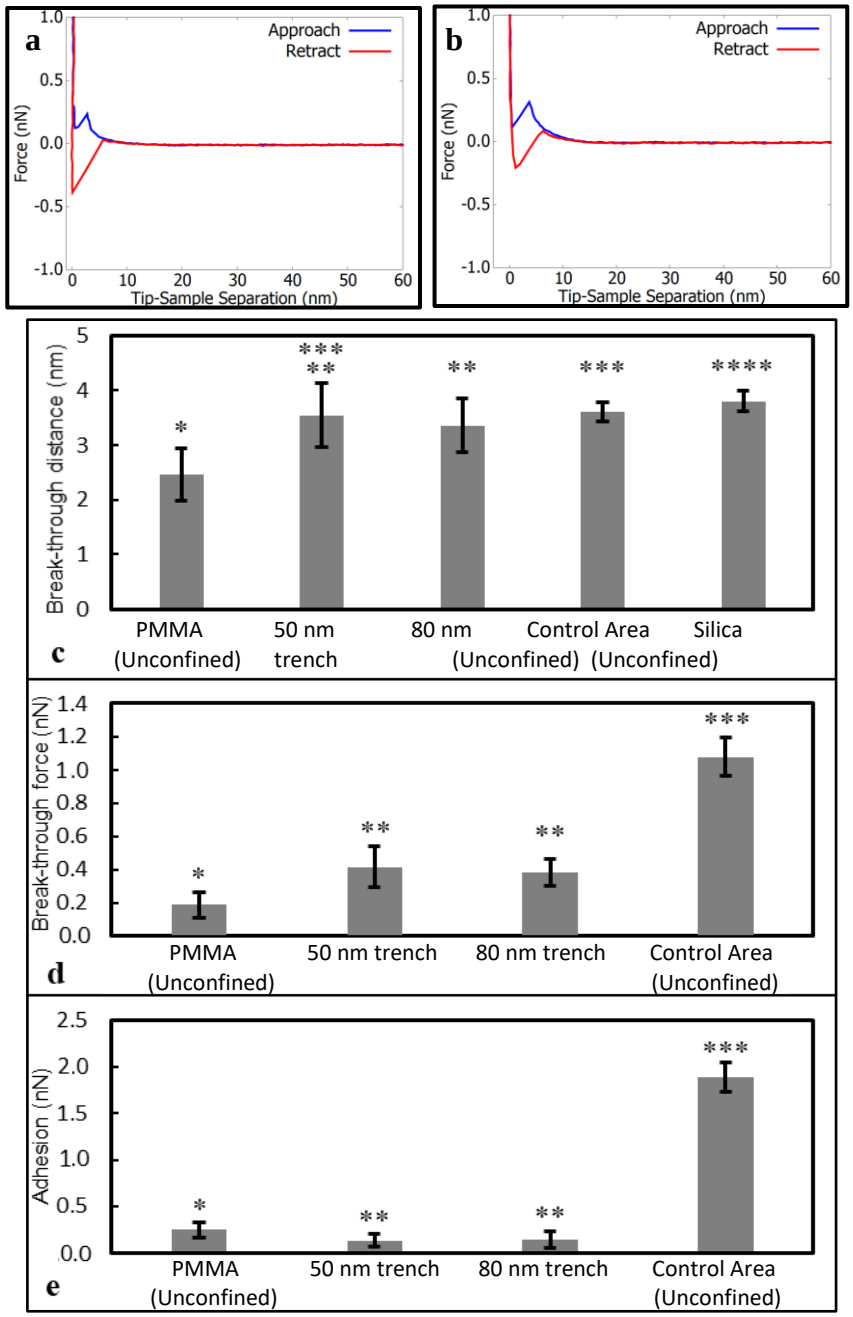

Figure 5. Force curves using 10×CMC TTAB on (a) unconfined PMMA and (b) in a 50 nm PMMA trench and (c) break-through distance, (d) break-through force and (e) adhesion force values collected from force maps in various locations. Stars represent statistically significant differences at the 95% confidence level.

Break-through values obtained from multiple force curves on unconfined PMMA, in the unconfined silica control area (which was previously covered with polymer) and from the 80 nm and 50 nm wide trenches are shown in Figure 5c-e. For all but the PMMA, the differences in break-through distances was slight (although statistically significant in some cases). PMMA had break-through distance about 2/3 of the other values. In our previous paper, we examined 3 surfaces with 3 different types of tips using TTAB and found no difference in average break-through distance above the CMC, even though surfaces were chosen to encompass both monolayers and bilayers. We had also found that the tips contained a monolayer of adsorbed surfactant.[1] The smaller break-through distance and force on PMMA are more consistent with monolayer adsorption than bilayer adsorption. Monolayer adsorption, to be consistent with our previous work, would indicate that no surfactant is being adsorbed by PMMA since tip adsorption appears as a monolayer. However, adsorption of cationic surfactants onto PMMA decrease the contact angle, consistent with significant surfactant adsorption.[24] The surface roughness of a polymer should be much larger than the hydrophobic graphite used previously and perhaps this roughness makes the adsorbed layer weak and irregular.

Break-through forces did vary with both surface and confinement. Force maps collected on the unconfined PMMA surface had the smallest break-through forces, about ½ of the 0.4 nN collected for the 50 and 80 nm trenches. The unconfined control areas had break-through values of ~1.1 nN. In our previous work on flat unconfined silica we found that an increase in break-through force occurred with an increase in surface concentration below the CMC.[1] Using those findings as a guide, the results presented in Figure 5 suggest confinement caused a reduction in the density of adsorbed surfactant which in turn was responsible for the reduction in break-through force. However, behaviors of adhesion forces were odd in two respects. First, the

adhesion force is typically larger than the break-through force (found for all samples in [1] and for CPC) but for the confined samples the adhesion force is smaller than the break-through force. Second, a decrease in adhesion force with decreasing surface density, as is found here, is expected; however, an increase in adhesion force was found previously in correspondence with a decrease in adsorbed surfactant density, which was explained as the effect of impurities.[1] Surfactant adsorption on and in the vicinity of the tip is complicated with respect to adhesion force measurements, and confinement of the walls may change this process.

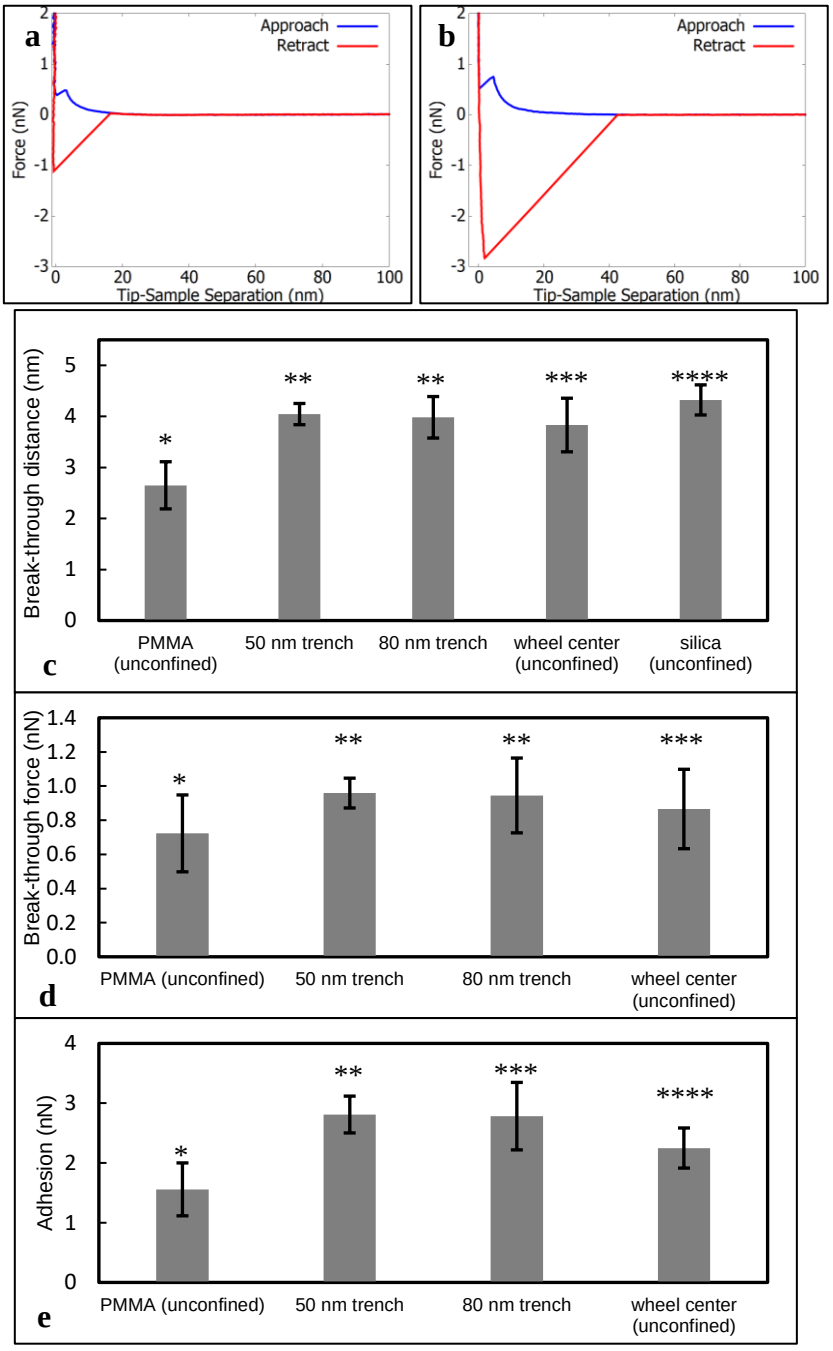

Figure 6. Force curves using 10×CMC CPC on (a) unconfined PMMA and (b) in a 50 nm PMMA trench and (c) break-through distance, (d) break-through force and (e) adhesion force values collected from force maps in various locations. Stars represent statistically significant differences at the 95% confidence level.

10×CMC CPC-PMMA

When the PMMA surfaces were submersed in 10×CMC CPC, there was no noticeable bubble formation until ~4 hours of exposure to the surfactant, slightly quicker

than with TTAB. However, as with TTAB, all data was collected at less than 3 hours after sample immersion. Figure 6c shows that on the PMMA surface the break-through distance was like that found for TTAB on the PMMA surface, approximately 2.4 nm. In this case, however, we have no data to indicate that CPC adsorbs on the AFM tip which means that this result could mean a CPC monolayer on PMMA, although the same explanation given for TTAB seems likely to be appropriate here as well. As seen with TTAB, the break-through distance increases on surfaces where the polymer was removed, reaching 3.7 - 3.9 nm for the trench floors and control area. The break-through force and adhesion values showed increases from the PMMA to the trenches (0.7 nN to 1.1 nN for break-through force and 1.5 nN to 2.8 nN for adhesion, respectively) but the value remained roughly the same between the trenches and the control area for the break-through force. Adhesion force values were smaller for the control area. The force behavior is markedly different for the CPC vs. the TTAB; the latter showed substantially higher forces for the control area than for the trenches. These results indicate that the identity of the surfactant can alter the effects of topological variations on surfactant adsorption.

Pillars

Figure 7a and Figure 7b show height and gradient maps. Gradient maps are generated from the uncorrected AFM signal to quickly determine whether adsorbed surfactant is on a surface and are more fully explained in our previous paper.[1] From the height map in Figure 7a, it is possible to distinguish between the upper surface of the nanostructure (light area), which was covered with metal mask during etching, and the lower surface (dark area), which was etched. The gradient map (Figure 7b) shows the edges between the upper surface and lower surface, but there is otherwise no significant variation in gradient across the individual surfaces indicating all regions had adsorbed surfactant.

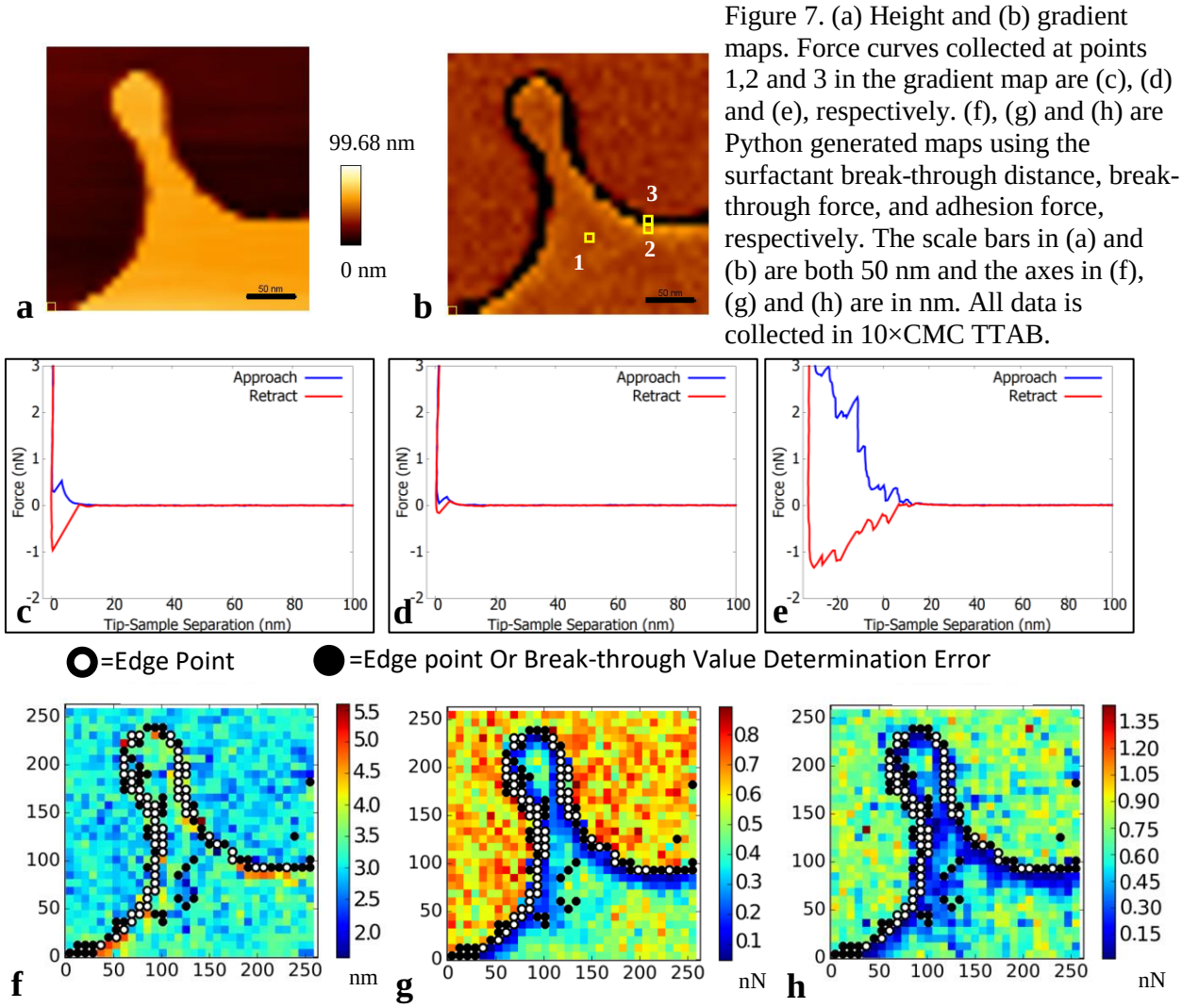

Figure 7. (a) Height and (b) gradient maps. Force curves collected at points 1,2 and 3 in the gradient map are (c), (d) and (e), respectively. (f), (g) and (h) are Python generated maps using the surfactant break-through distance, break-through force, and adhesion force, respectively. The scale bars in (a) and (b) are both 50 nm and the axes in (f), (g) and (h) are in nm. All data is collected in 10×CMC TTAB.

Figure 7c, d and e are representative force curves in the center of the structure (far from an edge), just before the edge, and on the edge, respectively. The curve collected in the center of the nano- structure shows a break-through force of 0.5 nN and an adhesion force of 1 nN. The force curve just before the edge shows significantly reduced break-through and adhesion forces. Because force curves on the edge were highly irregular and irreproducible, break-through values could not be determined. Other places, not on the edge, were also present in which the break-through values could not be determined, likely due to debris being present. Using these

guidelines, force-distance curves were grouped into curves on flat spots (colored squares), curves on edges (white circles with black edges), and curves where the break-through values could not be determined (black filled in circles). Hence, the edge was assigned as either the white circles with black edges, or, in some places consistent with visual inspection and Figure 7a and Figure 7b, black filled in circles.

Maps in Figure 7f, Figure 7g and Figure 7h were created according to the guidelines above to illustrate visually various adsorption characteristics. The break-through distance map in Figure 7f shows values between approximately 2.5 nm and 5 nm, typical values for TTAB adsorbed on silica.[1, 16, 25, 26] Near the edge the break-through distance values are higher than those farther into the interior of the structure. In the case of the break-through force and adhesion maps, Figure 7g and Figure 7h, respectively, forces increased (points go from yellow and light green to dark blue on the colormap scale) from the edge towards the interior. The break-through distance increase and forces decrease

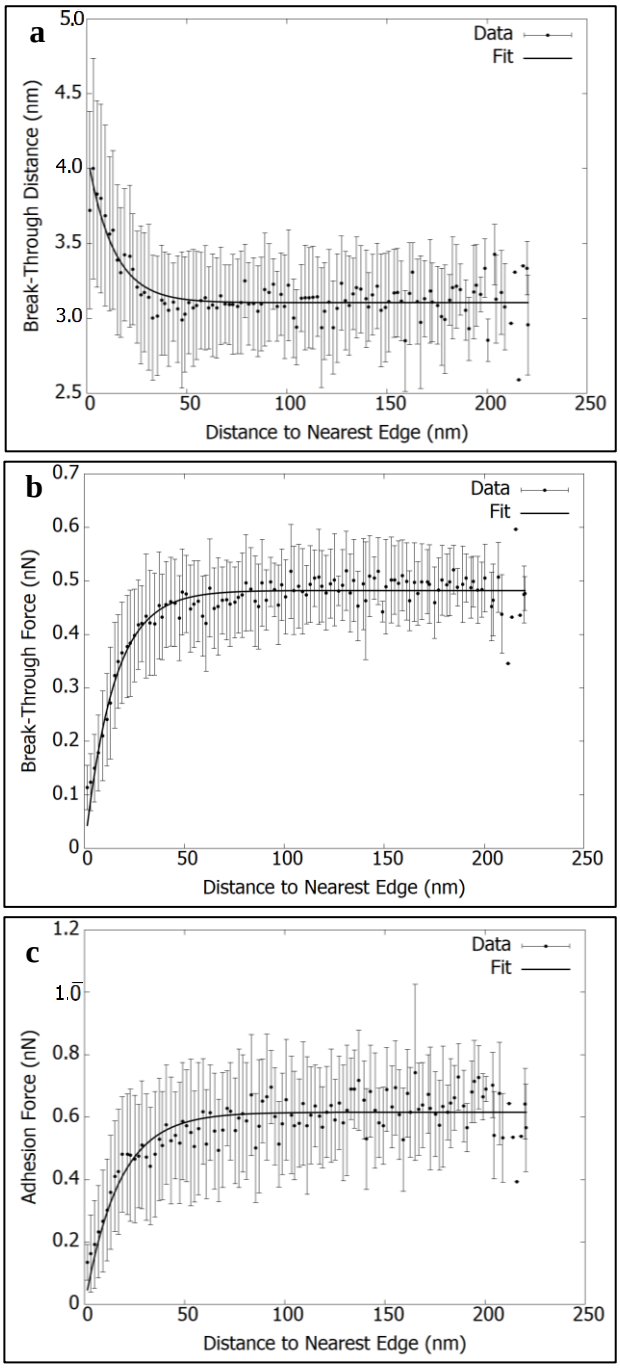

Figure 8. Break-through distance, break-through force and adhesion force vs. distance from the nearest edge

indicates a shift to an extended, less-dense hemifused layer near the edges of nano-pillars.

To quantitatively determine the relationship between break-through event values and distance to the nearest edge, the distance between a given force curve location and the closest edge point was determined. The procedure for finding the distance to an edge point from a specific map point was to iteratively draw a series of circles on the index, each having a radius of 0.1 nm larger than the last and determining the minimum radius where at least one edge point was touched by or encompassed in the circle. Break-through event values from these minimum radii were binned into 2 nm increments; averages and standard deviations are shown in Figure 8. All data was exponential in shape and therefore fit with the increasing or decreasing form of the exponential equation where y is the break-through value, x is the distance from the edge, τ is the decay length, and C and A are fitting constants.

$$y = Ce^{-x/\tau} + A \qquad \text{Decrease}$$

$$y = C(1 - e^{-x/\tau}) \qquad \text{Increase}$$

The results of the fit for the break-through distance are shown as black lines in each plot in Figure 8 and the fitting parameter values are shown in Table 1. Experiments were repeated using a second tip (plots not shown), and the same excellent exponential fit was found, albeit with differences in the fitting parameters, also shown in Table 1.

Table 1: Results of Exponential Fits to Curves Shown in Figure 8.

	Break-through distance			Break-through force		Adhesion force	
	C (nm)	A (nm)	τ (nm)	C (nN)	τ (nm)	C (nN)	τ (nm)
Tip 1	0.992 ±0.094	3.11 ±0.01	12.9 ±1.8	0.481 ± 0.003	14.5 ± 0.7	0.615 ± 0.007	17.1 ± 1.2
Tip 2	1.08	3.06	8.35	0.368	11.5	0.327	14.5

	±0.30	±0.02	±2.86	± 0.006	± 2.0	± 0.003	± 1.6

Differences between the distance at which the experimentally measured break-through force and break-through distance start to diverge from the constant value can be used to determine the probes' characteristic length (diameter for a hemispherical probe tip and width for a flat square tip). Three times (assuming 3τ captures the entire decay) the difference between the average break-through distance decay length and average break-through force decay length from Table 1 is ~7.5 nm. As shown in the SI, this value corresponds to the width of a flat square tip or to half the diameter of a hemispherical tip. Further, for a flat square tip, τ in Table 1 for the break-through distance does not include any tip convolution effects and the correct τ for the break-through force is the same as for the break-through distance. For a hemispherical tip, τ for the break-through distance minus ~2.5 nm is the correct decay length for both the force and the distance. Differences in decay lengths between the two forces is undoubtedly due to a rearrangement of adsorbed surfactant after the break-through event occurs. For justification for some assertions made here and further explanation of flat vs. circular tip please consult the SI.

Shown in Figure 9 are the wide variety of nanoscopic pillar shapes that were imaged; pillar characteristics did not measurably affect break-through distances or forces. However, differences among datasets would be difficult to discern because of the statistical uncertainty of the measurements coupled with the small number of data points for a specific shape.

In the previously mentioned molecular dynamic simulations of Suttipong, surfactant was shown to both form an aggregate that "turns the corner" of a step as well as forms only a single, slightly flat layer on the side of the step leaving the upper surface bare, depending on the height of the step.[12] The conclusion for both arrangements was that there is an energetic penalty to be

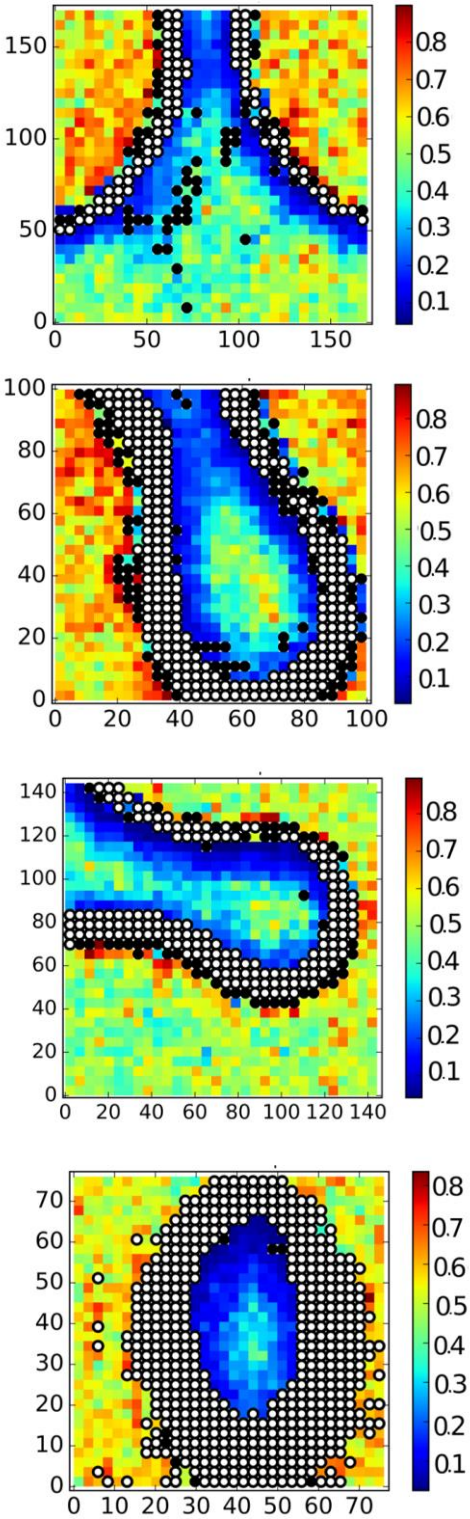

Figure 9. AFM Break-through force map on nanostructures of various shapes and sizes. White dots are edges, black are either edges or errors. All axes units are in nm.

paid in order to bend the surfactant layer around the edge, a conclusion similar to that reached by Liu et al., Fragneto et al., and Macakova et al. using rough surfaces.[2, 3, 7]

Qualitatively, our results are consistent with the former arrangement in Suttipong's simulations. We found that as distance to edge decreases the break-through distance increased and the break-through force decreased, consistent with the simulations where a less dense and stretched surfactant layer was formed on the corner of a step. However, quantitatively our results are different than those from simulations because experimentally the effects extend over much larger distances: tens of nanometers vs. ~7 nm in simulations. From the FFT of the soft contact image of TTAB on silica the repeat distance representing the worm-like micelle diameters was found to be 6.62 ± 0.70 nm, which is similar to the values for TTAB on quartz found by Berr.[6] Comparing our FFT dimensions with the decay length from the fitting means that the edge effects extend for many micelle diameters.

This work also shows that the type of confinement matters. Specifically, large changes in

adhesion force for TTAB adsorbed in trenches are much larger than the ~25% drop that would be expected based on the adhesion force measured on pillars 25 nm from the edge.

Conclusions

Effects of regular topological variations on adsorbed surfactant at the solid-liquid interface were investigated using AFM force mapping. Work presented here is, to our knowledge, the first experiment that measures surfactant adsorption on a surface with regular topological variations on a length scale small enough to be relevant to surfactant adsorption. With trenches, the cationic surfactant TTAB showed substantial reductions in break-through force and adhesion force with confinement while the cationic surfactant CPC showed a slight increase in these two forces with confinement. These results indicate that effects of topological variations can vary, depending on the surfactant. The break-through distance was not affected significantly by any changes in trench width, but was smaller on polymer vs. silica, indicating the break-through distance was affected by surface chemistry but not confinement.

AFM force mapping was also performed with TTAB adsorbed on the upper surface of nanoscopic pillar structures. Previous experimental work has shown that random topological variations lead to reductions in adsorbed surfactant amount and changes in morphology.[2-8, 23] In all cases break-through distance, break-through force and adhesive force data were well-described with a single exponential model. In agreement with coarse-grained simulations, an edge induces an extension of the surfactant molecules due to the micelles having to bend to cover the corner between the upper and side surfaces of the nanostructure.[12] Edges reduce surfactant adsorption for a few tens of nanometers, or several micelle diameters, from the edge itself. The fact that the adsorption amount decreases is not surprising, but the fact that adsorption decreases over such a long length scale is surprising because previous simulation

results found the reduction to extend less than ~7 nm from the edge.[12] The large lengths indicate the strong impact that cooperativity has on surfactant adsorption or, in other words, the strong impact that the exclusion of water from aliphatic tails has on surfactant adsorption.

One important next step is to reproduce these results using molecular dynamic simulations by changing the parameters used in the simulations while at the same time not changing any other surfactant behaviors that are correctly predicted by the simulations. Experimentally, cases where the angle of the edge is not 90° could be explored which would enable a better understanding of real surfaces which will have diverse nanometer-scale topological profiles. With respect to trenches, we had planned to report results using different surface chemistry for the walls but were unable to complete the experiments.

Acknowledgements

The authors thank Dale Teeters and Paige Johnson for their assistance in manufacturing the trenches, Matt Johnson and Rassel Shazzad for their assistance in manufacturing the pillars, and Preston Larson for electron microscopy assistance. Primary financial support was provided by the National Science Foundation under Grant No. CMMI–1068705 as well the American Australian Association for funding JJH to spend a year in Australia through the Sir Keith Murdoch fellowship. We would also like to thank support from the U.K. Engineering and Physical Sciences Research Council under grant number EP/N007123/1 to AS, an ARC Future Fellowship (FT160100191) to RFT. This work was performed in part in the Materials Characterization and Fabrication Platform (MCFP) at the University of Melbourne with the help of Matthew Bivano and Dr. Christine Browne. Also, BPG and JJH would like to thank the industrial sponsors of the Institute for Applied Surfactant Research (IASR) at the University of Oklahoma (BASF, Church & Dwight, Clorox,

Colgate-Palmolive Company, Ecolab, ExxonMobil, Huntsman Corporation, Procter & Gamble, Sasol (USA) Corporation, Shell Global Solutions (US) Inc.).

Supporting Information

Supporting information contains detailed AFM tip descriptions, procedures used to manufacture the trenches and pillars, as well as some information on their characteristics, a discussion of convolution effects and finally a discussion of the reason for the choice of surfactants.

References

[1] J.J. Hamon, R.F. Tabor, A. Striolo, B.P. Grady, Langmuir 34 (2018) 7223.

[2] G. Fragneto, R.K. Thomas, A.R. Rennie, J. Penfold, Langmuir 12 (1996) 6036.

[3] L. Macakova, E. Blomberg, P.M. Claesson, Langmuir 23 (2007) 12436.

[4] S.Q. Wu, L. Shi, L.B. Garfield, R.F. Tabor, A. Striolo, B.P. Grady, Langmuir 27 (2011) 6091.

[5] C. Gutig, B.P. Grady, A. Striolo, Langmuir 24 (2008) 13814.

[6] J.C. Schulz, G.G. Warr, Langmuir 18 (2002) 3191.

[7] J.-F. Liu, W.A. Ducker, J. Phys. Chem. B 103 (1999) 8558.

[8] H.C. Schniepp, H.C. Shum, D.A. Saville, I.A. Aksay, J. Phys. Chem. B 111 (2007) 8708.

[9] N.R. Tummala, A. Striolo, ACS Nano 3 (2009) 595.

[10] N.R. Tummala, B.P. Grady, A. Striolo, PCCP 12 (2010) 13137.

[11] M. Suttipong, B.P. Grady, A. Striolo, J. Phys. Chem. B 119 (2015) 5467.

[12] M. Suttipong, B.P. Grady, A. Striolo, Soft Matter 13 (2017) 862.

[13] M. Marquez, K. Patel, A.D.W. Carswell, D.W. Schmidtke, B.P. Grady, Langmuir 22 (2006) 8010.

[14] S. Manne, J.P. Cleveland, H.E. Gaub, G.D. Stucky, P.K. Hansma, Langmuir 10 (1994) 4409.

[15] H.N. Patrick, G.G. Warr, S. Manne, I.A. Aksay, Langmuir 13 (1997) 4349.

[16] S.B. Velegol, B.D. Fleming, S. Biggs, E.J. Wanless, R.D. Tilton, Langmuir 16 (2000) 2548.

[17] A. Blom, G.G. Warr, E.J. Wanless, Langmuir 21 (2005) 11850.

[18] E.J. Wanless, W.A. Ducker, J. Phys. Chem. 100 (1996) 3207.

[19] B.D. Fleming, S. Biggs, E.J. Wanless, J. Phys. Chem. B 105 (2001) 9537.

[20] E.J. Wanless, T.W. Davey, W.A. Ducker, Langmuir 13 (1997) 4223.

[21] E.J. Wanless, W.A. Ducker, Langmuir 13 (1997) 1463.

[22] T.J. Senden, C.J. Drummond, P. Kekicheff, Langmuir 10 (1994) 358.

[23] H.C. Schniepp, H.C. Shum, D.A. Saville, I.A. Aksay, J. Phys. Chem. C 112 (2008) 14902.

[24] A. Zdziennicka, B. Janczuk, J. Colloid Interf. Sci. 350 (2010) 568.

[25] J.-F. Liu, G. Min, W.A. Ducker, Langmuir 17 (2001) 4895.

[26] J. Li, C. Zhang, P. Cheng, X. Chen, W. Wang, J. Luo, Langmuir 32 (2016) 5593.